International Journal of
MATERIALS RESEARCH

Zeitschrift für METALLKUNDE

Original Contributions

Ming Wei[a], Lijun Zhang[a], Mingjun Yang[a], Kai Li[a], Shuhong Liu[a], Pizhi Zhao[b], Yong Du[a]
[a] State Key Lab of Powder Metallurgy, Central South University, Changsha, P.R. China
[b] Chinalco Research Institute of Science and Technology Co., Ltd., Beijing, P.R. China

Phase-field simulation of the solidified microstructure in a new commercial 6××× aluminum alloy ingot supported by experimental measurements

This work attempts to quantitatively describe the microstructural evolution in a new commercial 6××× aluminum alloy developed in an industrial laboratory (Al-0.87Si-0.81Mg-0.51Zn-0.46Cu-0.19Fe-0.09Mn, in wt.%), during solidification by using the phase-field simulation supported by experimental measurements. Coupling to the CALPHAD thermodynamic and atomic mobility databases is attained for providing energy and diffusivity information during the phase-field simulation. Two different resolutions are used in order to resolve the primary α-(Al) dendrite and the faceted β-AlFeSi eutectic phase in the phase-field simulations. The phase-field simulated microstructure morphology is verified by experimental results. Moreover, the microsegregation and back-diffusion phenomena in the primary α-(Al) dendrite are also analyzed.

Keywords: 6××× aluminum alloy; Phase-field simulation; CALPHAD; Solidification; Microstructure

1. Introduction

Aluminum alloys have been widely applied in automotive, construction, aerospace, and other fields due to their excellent performance [1, 2]. 6××× Al–Mg–Si–Cu-based aluminum wrought alloys inherently possess ideal formability, corrosion stability, weldability, high fatigue strength, as well as medium static strength and are thus the preferred choice for automobile body panels [3, 4]. As one of the typical representatives, AA6016 aluminum alloy has been used for the body panels of the Audi A8 aluminum car [5, 6].

Smelting and casting is the initial work stage during the preparation of the aluminum alloys. The solidification behavior of the ingot has an inherent influence on its microstructural evolution during the subsequent heat treatments and on its final performance [7–9]. Therefore, in order to assist the design of novel aluminum alloys, a fundamental understanding of the microstructure of the target during solidification, such as the morphology and distribution of primary dendrite and intermetallic compounds, the segregation of solute elements, and the secondary dendrite arm spacing (SDAS), etc., is essential. Due to the unavoidable addition of Fe in an industrial smelting process, β-AlFeSi usually forms and represents a typical harmful phase in aluminum alloys [10–12]. In order to impede the effect of β-AlFeSi on aluminum alloys, its related microstructure description is a prerequisite.

The experimental investigation of the solidified microstructure is straightforward and is commonly the first choice for material analysis. However, conducting a pure experiment is time-consuming and it is difficult to reproduce the entire transformation process for commercial aluminum alloys, which are usually comprised of multiple

components and multiple phases. In order to gain an insight into the complex microstructural evolution in target alloys during solidification, an advanced computational technique is an appropriate fundamental tool.

The phase-field method that was developed over the past twenty years has been widely applied to describe the microstructural evolution in different alloys during solidification [13–18]. The simulation of the microstructural evolution in multi-component, multi-phase alloys during solidification has become more feasible with the development of the multi-phase-field (MPF) model by Steinbach and his coworkers [17, 19, 20]. Based on the MPF model, the commercial phase-field simulation software package MICRESS (MICRostructure Evolution Simulation Software) [21] was developed. Moreover, its linking to the CALPHAD (CALculation of PHAse Diagram) thermodynamic and kinetic databases has become feasible through the TQ interface [22, 23]. The thermodynamic database provides energy-related information such as chemical/diffusion potentials, driving force, and so on, while the kinetic database provides accurate diffusivity information. In addition to the input of accurate thermodynamic and thermophysical parameters, an experimental validation is also an indispensable element for quantitative phase-field simulation [24].

To date, some reports [25–29] on the phase-field simulation of the microstructural evolution in commercial aluminum alloys during solidification by using MICRESS have been published. However, it is still very difficult to accurately resolve the dendritic primary phase and the eutectic structure simultaneously using a uniform resolution as a single open problem in the current phase-field simulation of the solidified microstructure. Much computational cost is required and the computational efficiency will be low if a high resolution is applied in view of the very small eutectic structure. In contrast, the subtle morphology of some eutectic phases, e. g. β-AlFeSi, cannot be described adequately if a low resolution is applied in view of computational efficiency/cost.

Consequently, this study aims to perform a phase-field simulation of the microstructural evolution in the new 6××× commercial aluminum alloy ingot developed at the Chinalco Research Institute of Science and Technology Co., Ltd. during solidification by using MICRESS supported by key experimental measurements. The integration with reliable thermodynamic and atomic mobility databases is conducted for providing accurate energy and diffusivity information during the phase-field simulation. We focus on the growth process of the primary α-(Al) dendrite and faceted β-AlFeSi eutectic phase in this 6××× alloy ingot during solidification. Separate phase-field simulations with two magnitudes of resolution are performed to resolve the primary dendrite and β-AlFeSi phase in the solidified microstructure. Moreover, based on the phase-field simulated results, the microsegregation and back-diffusion phenomena in the primary α-(Al) dendrite are also analyzed.

2. Experimental procedure

The new 6××× alloy ingot was melted in a graphite crucible in an electrical resistance furnace. The nominal composition of this 6××× alloy is Al-0.87Si-0.81Mg-0.51Zn-0.46 · Cu-0.19Fe-0.09Mn (in wt.%), which is close to AA6016. A pure aluminum ingot and Al–X (X = Si, Mg, Cu, Zn) master alloy ingots of industrial purity 99.9 % were chosen as the raw material. Subjected to two cycles of slagging and degassing, the liquid melt was poured into a crystallizer to obtain the ingot. The size of the ingot was 350 mm × 230 mm × 60 mm.

Afterwards, the cubic specimens with the size of 10 mm × 10 mm × 10 mm were cut off from the center of the ingot at which the cooling rate was 0.6 K s^{-1}. After grinding and polishing, the specimens were measured by a scanning electron microscope (SEM) (FEI Helios NanoLab) and a metallographic microscope (Leica D-35578 Wetzlar) after being corroded by Keller etchant (1.0 ml HF, 1.0 ml HCL, 3.0 ml HNO_3, 95 ml H_2O) for 10 s.

3. Phase-field model and input of material parameters

3.1. Multi-phase-field model

For the solidification process, the total free energy functional can be generally split into interfacial energy f^{intf} and chemical energy f^{chem} [17, 20]:

$$F = \int_{\Omega} f^{\text{intf}} + f^{\text{chem}} \tag{1}$$

$$f^{\text{intf}} = \sum_{\alpha,\beta=1,\ldots,N,\alpha\neq\beta} \frac{4\sigma_{\alpha\beta}}{\eta_{\alpha\beta}} \left\{ \frac{\eta_{\alpha\beta}^2}{\pi^2} \nabla\phi_\alpha \nabla\phi_\beta + \phi_\alpha\phi_\beta \right\} \tag{2}$$

$$f^{\text{chem}} = \sum_{\alpha=1,\ldots,N} h(\phi_\alpha) f_\alpha(c_\alpha^i) + \tilde{\mu}^i \left(c^i - \sum_{\alpha=1,\ldots,N} \phi_\alpha c_\alpha^i \right) \tag{3}$$

where $N = N(x)$ is the local number of phases and the sum constraint $\sum_{\alpha=1,\ldots,N} \phi_\alpha = 1$ is always fulfilled; ϕ_α is the phase-field value of α phase/grain; $\sigma_{\alpha\beta}$ is the interfacial energy between phases/grains α and β; $\eta_{\alpha\beta}$ is the interfacial width; $h(\phi_\alpha)$ is a monotonous coupling function; $f_\alpha(c_\alpha^i)$ is the bulk free energy density of the individual phase, which depends on the phase concentration c_α^i; and $\tilde{\mu}^i$ is the diffusion potential of component i introduced as a Lagrange multiplier to conserve the mass balance between the phases $c^i = \sum_{\alpha=1,\ldots,N} \phi_\alpha c_\alpha^i$.

Based on the free energy functional shown in Eqs. (1–3), the governing equations for the phase field and concentration can be derived based on the above free energy function [20]:

$$\dot{\phi}_\alpha = -\sum_{\beta=1}^{\tilde{\nu}} \frac{u_{\alpha\beta}}{\tilde{\nu}} \left(\frac{\delta F}{\delta\phi_\alpha} - \frac{\delta F}{\delta\phi_\beta} \right) \tag{4}$$

$$\dot{c}^i = \nabla \sum \phi_\alpha M_\alpha \nabla\tilde{\mu}_\alpha^i \tag{5}$$

where $u_{\alpha\beta}$ is the physical mobility between phase α and β; and $\Delta g_{\alpha\beta}$ is the local deviation from the thermodynamic equilibrium. It should be noted that the chemical driving force $\Delta g_{\alpha\beta}$ can be obtained by linking to the accurate CALPHAD thermodynamic databases. M_α is the chemical mobility in phase α and can be also directly obtained from the CALPHAD atomic mobility databases.

In order to achieve a low computation time, the interface width is often chosen to be much larger than the physical interface width in a realistic phase-field simulation. However, when the numerical interface width is applied to simulate the solidification process, it will suffer from an anomalous chemical potential jump at the interface [30, 31] due to the unequal thermal properties such as diffusivities and conductivities. The anomalous jump is caused by the so-called numerical solute trapping effect [32]. The first step to eliminate the numerical solute trapping effect is to introduce an effective interface mobility instead of a physical interface mobility in the phase-field equation [17], which was applied in this simulation. The second step is to introduce an anti-trapping current term in the diffusion equation, which was first achieved by Karma [33] and was later extended by Kim [34], Gopinath et al. [35], Ohno and Matsuura [36], Pan and Zhu [37], and also Carre et al. [38]. Very recently, Boussinot and Brener [39] and Fang and Mi [40] derived an anti-trapping phase-field model that was thermodynamically consistent. Although the numerical solute trapping effect can be nicely reduced with these models, only phenomenological [33–38] or thermodynamically consistent [39, 40] anti-trapping phase-field models can be applied to binary and multicomponent two-phase cases and are thus not applicable in the present multicomponent multiphase case.

3.2. CALPHAD database coupling

As described above, the CALPHAD-type thermodynamic and atomic mobility databases can provide the thermodynamic and diffusivity information required for the phase-field simulation of a multi-component multi-phase commercial aluminum alloy. The crucial databases employed in this work have been established by our research group. The thermodynamic database of the Al alloys [41] includes 34 elements and thermodynamic descriptions of up to 445 phases, including liquid phases, all the solid solution phases, and intermetallic compounds. The atomic mobility database [42, 43] contains 34 elements and the mobility descriptions of the liquid and solid solution phases.

According to the thermodynamic database of the Al alloy [41], in the Al-rich Al–Si–Mg–Zn–Cu–Fe–Mn system, the liquid and α-(Al) are treated as solution phases, Al_2Cu (θ), Mg_2Si, and $Al_{16}FeMn_3$ are compounds described by the sublattice model, while (Si), α-AlFeSi (α), and the β-AlFeSi (β) phases are stoichiometric phases. The constitutions Al_8Fe_2Si and $Al_9Fe_2Si_2$ are chosen for the α-AlFeSi and β-AlFeSi phases in the thermodynamic database [41] and are thus utilized in the present phase-field simulation.

3.3. Material parameters and initial settings

We assumed the growth of all phases to be diffusion-controlled. The interfacial mobility was generally formulated in the thin-interface limit as illustrated by Steinbach [17]. The mean value of the interfacial energy of the liquid and α-(Al) was 0.16 J m^{-2} based on the study by Gunduz and Hunt [44]. The interfacial energies for liquid/β-AlFeSi and α-(Al)/β-AlFeSi were estimated to be 0.2 J m^{-2} and 0.5 J m^{-2}, respectively.

The boundary conditions for the phase field and concentration were set to be periodic. Moreover, the cooling rate was set to be consistent with the experimental condition, i. e., 0.6 K s^{-1}. The initial temperature was 918 K with an undercooling of 5 K. The anisotropic coefficient for α-(Al) was set to 0.1 and the β-AlFeSi particle was set as a (001) faceted morphology.

4. Results and discussion

Figure 1 shows a backscattered electron image (BSE) of the solidified microstructure of this new 6××× aluminum alloy ingot. The gray area is primary α-(Al). The white area is eutectic mixture that contains Fe or Cu. As can be seen, the eutectic mixture mainly distributes along the elongated grain boundary and locates in the α-(Al) grain, appearing as a nearly round structure. Among the eutectic phases, the black area is Mg_2Si, while the platelet white structure located along the boundaries is the β-AlFeSi phase.

The solidification sequence of the alloy was first predicted by the Scheil–Gulliver solidification model based on the thermodynamic database [41] and the result is shown in Fig. 2. As can be seen, the predicted solidification sequence is:

$$\mathrm{L} \rightarrow \alpha - (\mathrm{Al}) \tag{6}$$

$$\mathrm{L} \rightarrow \alpha - (\mathrm{Al}) + \alpha - \mathrm{AlFeSi} \tag{7}$$

$$\mathrm{L} \rightarrow \alpha - (\mathrm{Al}) + \alpha - \mathrm{AlFeSi} + \beta - \mathrm{AlFeSi} \tag{8}$$

$$\mathrm{L} \rightarrow \alpha - (\mathrm{Al}) + \alpha - \mathrm{AlFeSi} + \beta - \mathrm{AlFeSi} + \mathrm{Mg_2Si} \tag{9}$$

$$\mathrm{L} \rightarrow \alpha - (\mathrm{Al}) + \alpha - \mathrm{AlFeSi} + \beta - \mathrm{AlFeSi} + \mathrm{Mg_2Si} + (\mathrm{Si}) + \mathrm{Al_{16}FeMn_3} \tag{10}$$

$$\mathrm{L} \rightarrow \alpha - (\mathrm{Al}) + \alpha - \mathrm{AlFeSi} + \beta - \mathrm{AlFeSi} + \mathrm{Mg_2Si} + (\mathrm{Si}) + \mathrm{Al_{16}FeMn_3} + \mathrm{Al_2Cu} \tag{11}$$

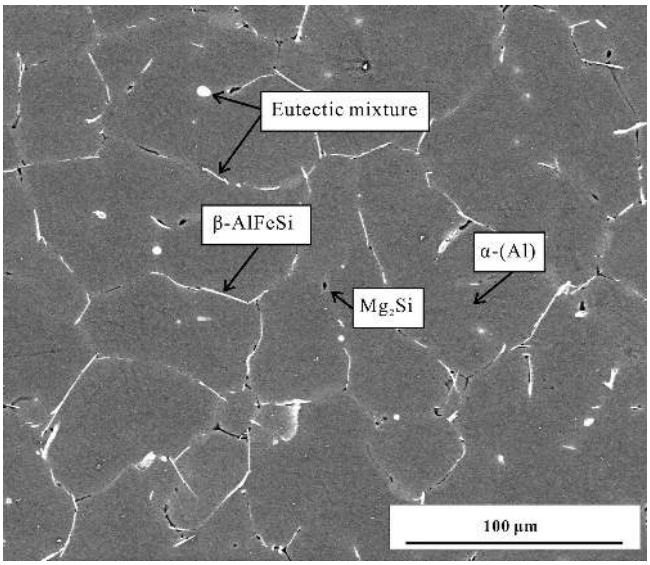

Fig. 1. Cast microstructure (BSE image) of the 6××× alloy ingot.

Based on the Scheil–Gulliver simulation, it is found that β-AlFeSi, α-AlFeSi, (Si), and the Mg_2Si phases are involved in the respective binary, ternary, quaternary, and quinary eutectic structures. It should be noted that the solidified microstructure in the alloy predicted from the Scheil–Gulliver simulation is consistent with the experimental observation, further confirming the reliability of the present thermodynamic database.

As described in Section 1, it is very difficult to explain the details of the primary and the eutectic phases with the same resolution in one phase-field simulation. Thus, two separate phase-field simulations were performed, one for the solidification of the primary α-(Al) and the other for the growth process of the β-AlFeSi phase in the eutectic structure.

Figure 3a–h presents the two-dimensional (2-D) phase-field simulation results of the growth and coarsening process of the primary α-(Al) dendrite of the alloy during solidification. For consistency with the experimental microstructure, a simulation domain with a size of 350 μm × 350 μm was chosen for the phase-field simulation of the primary α-(Al) dendritic growth. In order to increase the computational efficiency, a grid spacing of 1 μm was fixed. Figure 3i is a metallographical image of the 6××× alloy in-got after etching by Keller's reagent, which was included here for a direct comparison with the phase-field simulated results. As can be seen in Fig. 3, the growth and coarsening process of the primary α-(Al) dendrite is well reproduced by the phase-field simulation at the mesoscale. Typical secondary dendrites form at the initial stage of solidification under the action of combined anisotropy and become obtuse during the coarsening process. This results in a clear nearly round structure forming in the grain as shown in Fig. 3 and verified in Fig. 1. By combining with the solute distribution information in Fig. 4, the eutectic reaction should happen first in these isolated round structures because the exchange of the solute in the liquid is impeded.

According to the phase-field simulations, the solidification rate curve, i. e., the mass fraction of the solidified solids *fs* versus the temperature can also be plotted and superimposed in Fig. 2. As is evident in the figure, the phase-field simulated solidification rate curve is lower than the curves predicted from the equilibrium calculation and the Scheil–Gulliver simulation at the beginning of the solidification because the undercooling is considered only in the phase-field simulation. Moreover, as the solidification continues, the phase-field simulated solidification rate curve is located between the curve of the equilibrium calculation and the

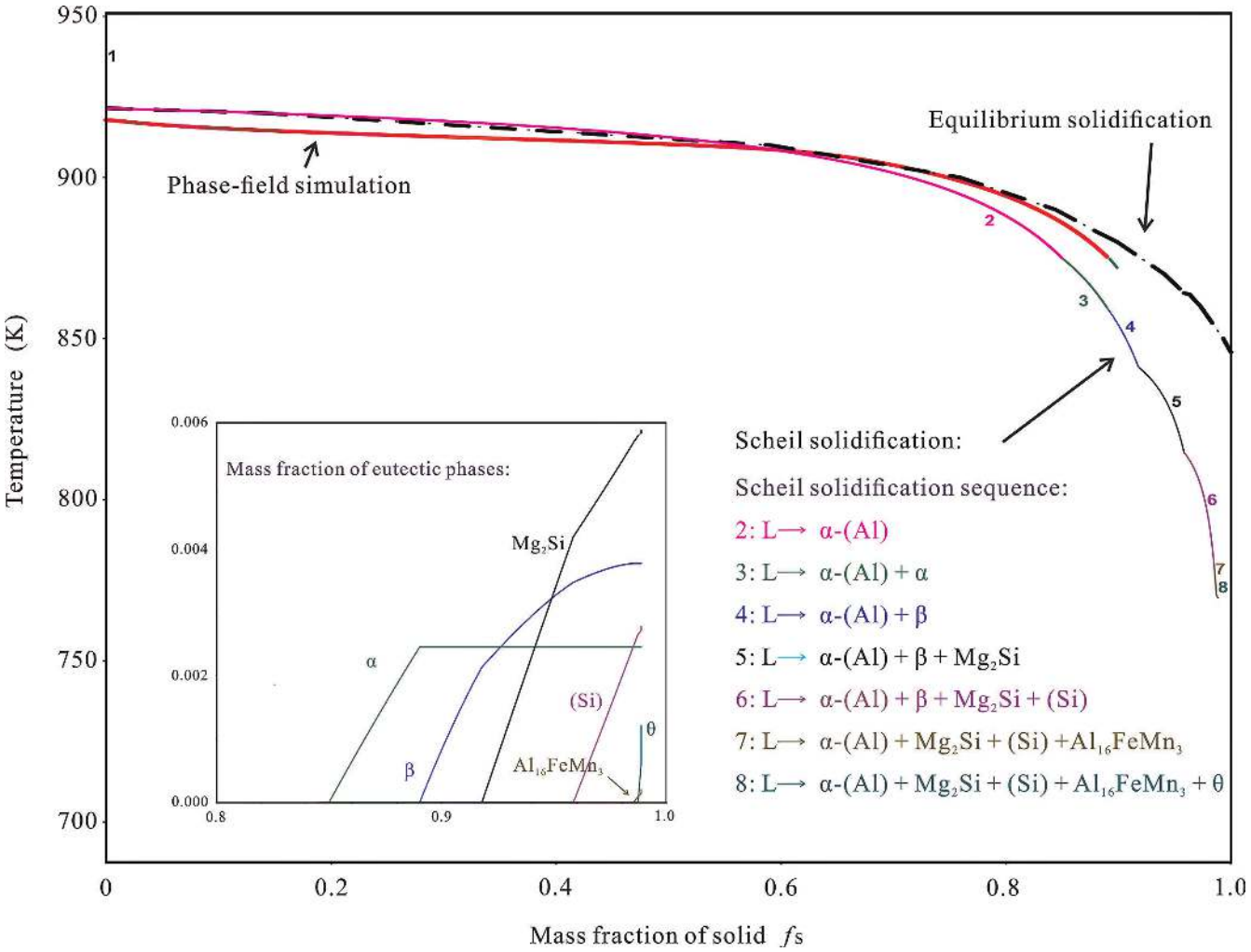

Fig. 2. Solidification sequence of the 6××× alloy in the Scheil model and the changes in solid fraction versus temperature in the equilibrium solidification, the Scheil solidification, and the phase-field simulation. α, β, and θ denote the α-AlFeSi, β-AlFeSi, and Al_2Cu phases, respectively.

curve based on the Scheil–Gulliver simulation. This occurs due to the different assumptions for the diffusion in liquids and solids for different models. For the equilibrium calculation, the diffusion is assumed to be infinite in both the liquid and the solid phases. For the Scheil simulation, the diffusion in the liquid is infinite while no diffusion is taken into account for the solid phases. In the phase-field simulation, the diffusion is finite in both the liquid and the (Al) phases and their diffusivities are based on the reliable atomic mobility databases [42, 43].

Figure 4 shows the heterogeneous distribution of Si and Fe in the primary α-(Al) dendrite and the residual liquid. As can be seen in Fig. 4, there is a clear gradient of Si and Fe in the α-(Al) dendrite, i. e., the concentration is much larger near the solid–liquid interface than at the center of the dendrite. Furthermore, we can find that Fe has a small solubility in α-(Al) and thus Fe gathers in the liquid, resulting in the formation of a series of Fe-compounds along the grain boundaries of α-(Al).

Figure 5 shows the back-diffusion phenomenon in the α-(Al) dendrite, which may influence its microsegregation, and then even the solidification sequence, forming microstructure and mechanical properties of the target alloy. The dotted lines demonstrate the change in the solute concentrations of Cu and Zn at the dendrite tip as the temperature decreases, while the solid lines show the change in the solute

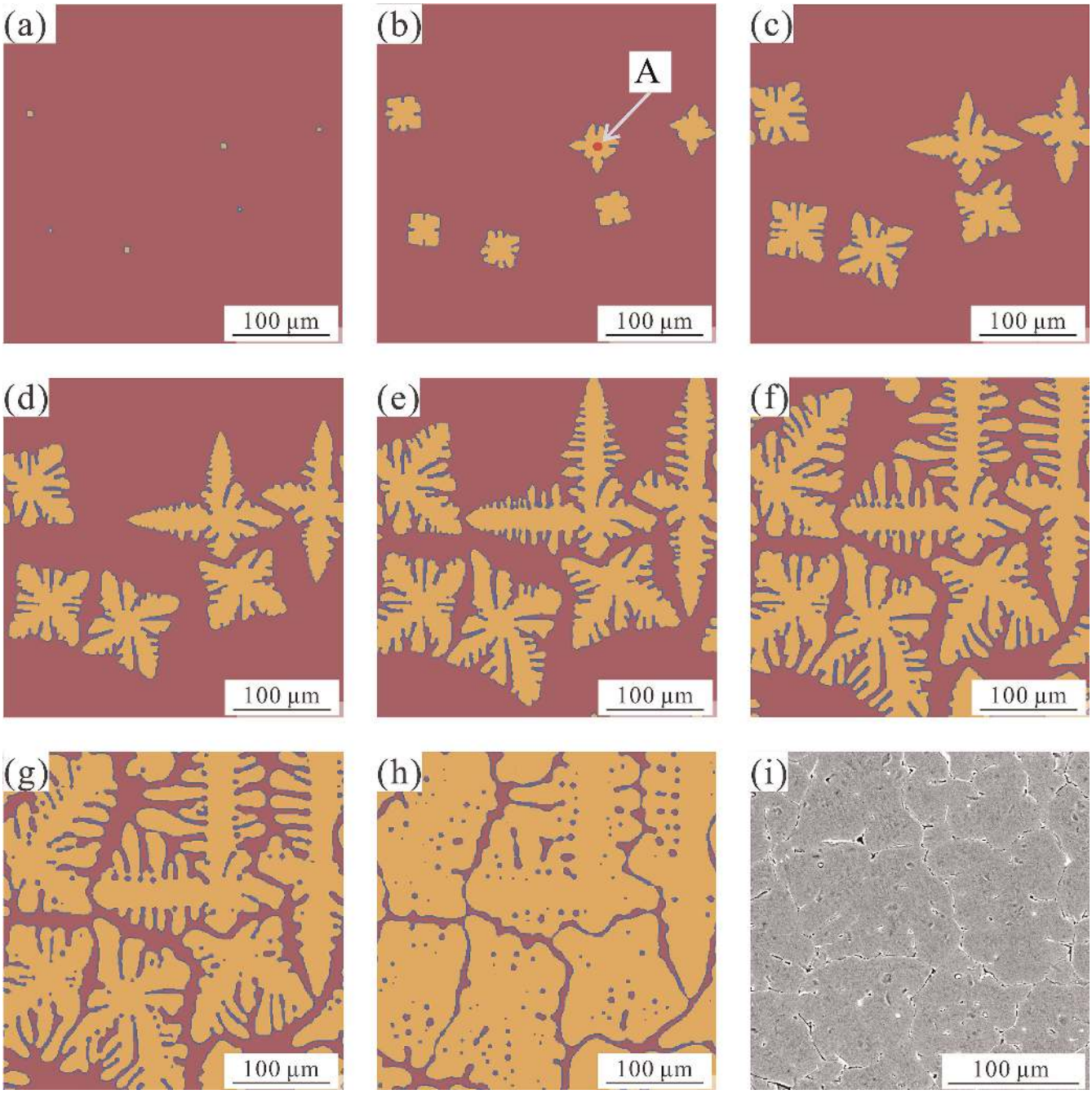

Fig. 3. Phase-field simulation of the dendritic growth and coarsening process of the α-(Al) dendrite and a comparison with the experimental result. (a) 918 K, (b) 916.2 K, (c) 914.4 K, (d) 913.2 K, (e) 911.4 K, (f) 908.4 K, (g) 902.4 K, (h) 870 K, (i) experimental result. The red point A in (b) denotes the position of a nucleus.

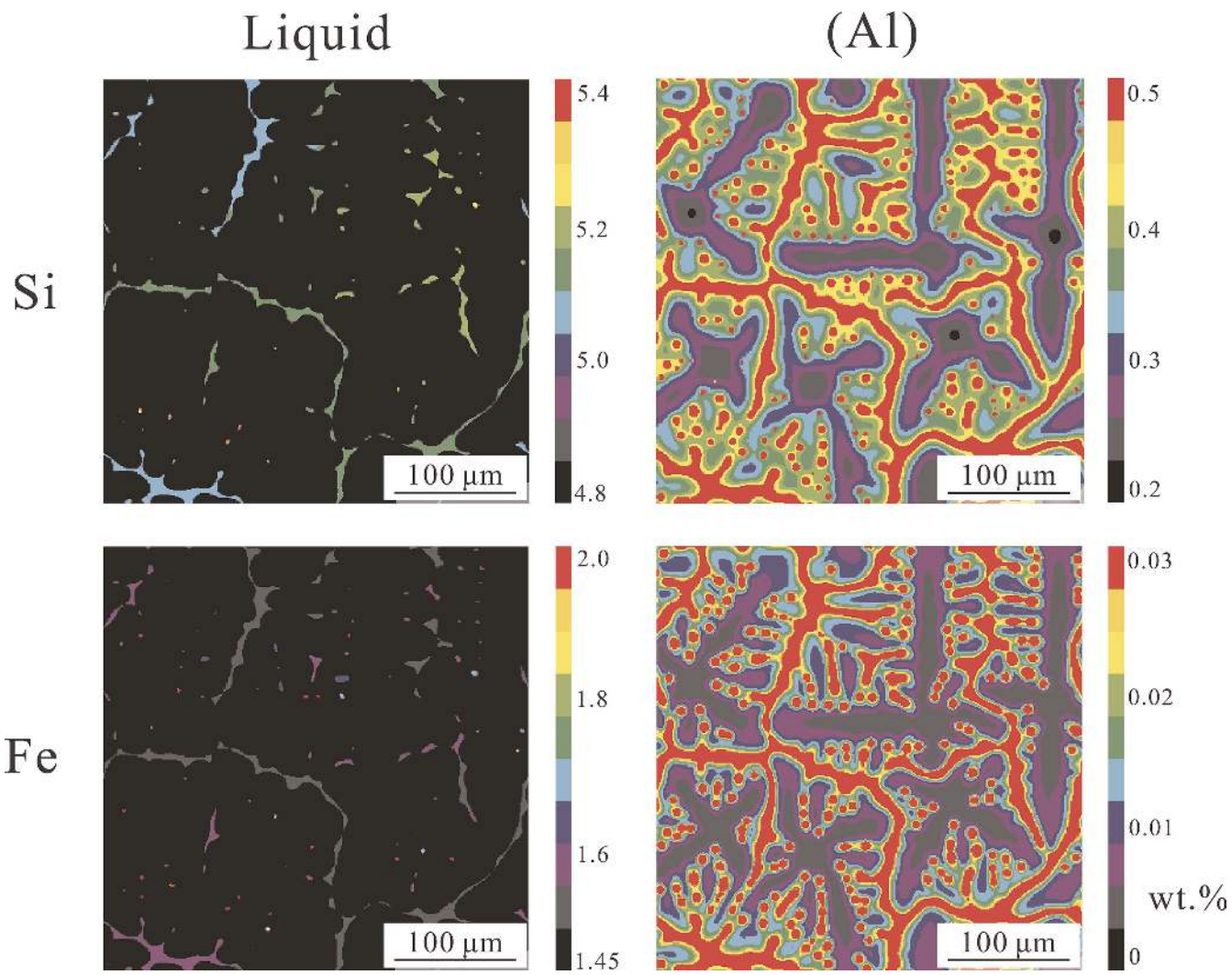

Fig. 4. Distribution of Si and Fe in the primary α-(Al) dendrite and residual liquid.

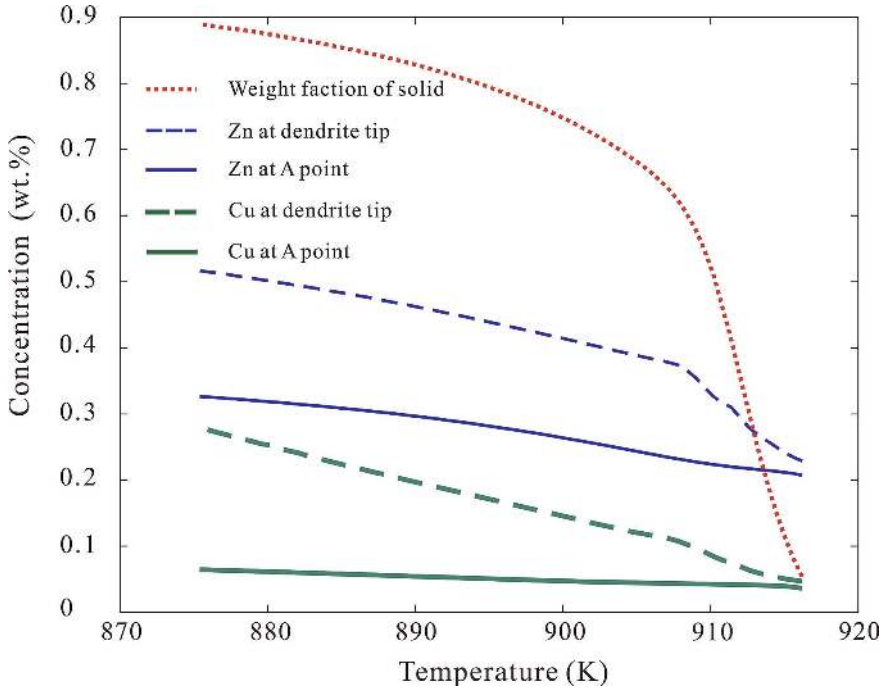

Fig. 5. Changes in Cu and Zn concentration at point A versus temperature due to back diffusion.

concentrations of Cu and Zn at point A marked in Fig. 3b (i.e., the position of an initial nucleus). As can be seen, the solute concentrations at the dendrite tip increase consistently prior to the eutectic reaction because of the solute enrichment in the liquid; their increase in speed has an obvious relationship with the dendritic growth rate. Generally, the concentration of Cu and Zn at point A keeps increasing during the solidification but the increase is more pronounced for Zn than for Cu due to the larger diffusion coefficient of Zn in the α-(Al) matrix.

The initial state for the phase-field simulation of β-AlFeSi is shown in Fig. 6a. The simulation domain has a size of 7 μm × 20 μm with a grid spacing of 0.05 μm. It starts from the primary α-(Al) phase and the remainder liquid based on the phase-field simulation results with lower resolution (i.e., 350 μm × 350 μm with a grid spacing of 1 μm) at the last step (i.e., at 870 K). The initial concentrations of the liquid and (Al) are set to be the same as those of the corresponding phases near the interface in the simulation with the lower resolution and are treated as constants for simplification for the subsequent simulation with higher resolution. Moreover, the fractions of the (Al) and liquid phases at the initial state of the phase-field simulation with higher resolution are identical to those with the lower resolution. The values of the other parameters, including temperature, thermodynamics, diffusivities, interface energy, and interface mobility are identical to those of the phase-field simulation with the lower resolution. In additional, a nucleus of the β-AlFeSi phase (white) with a radius of 1 μm is pre-set in the residual liquid (red) between the two primary α-(Al) grains. The β-AlFeSi phase is treated as a stoichiometric phase and the crystal structure of the β-AlFeSi phase is clinorhomboidal [11, 45].

Based on these input, the growth process of the β-AlFeSi phase is reproduced by using the phase-field simulation, as displayed in Fig. 6a–d. In the simulation, β-AlFeSi represents a (001) faceted morphology, which is coincident with the experimental structure shown in Fig. 6f. The average transverse growth velocity of the β-AlFeSi particles is 0.11 μm s^{-1}, which is located exactly in the experimentally observed range of 0.08 μm s^{-1}–20 μm s^{-1} [46]. Moreover, in this phase-field simulation, we observed a slight increase in the thickness of the β-AlFeSi plate during the transverse growth process. A similar phenomenon was also observed in the in-situ experiment by Terzi et al. [47].

5. Conclusions

A phase-field simulation supported by experimental measurements was employed to investigate the microstructural evolution in a new commercial 6××× aluminum alloy during solidification. The integration with the CALPHAD thermodynamics and atomic mobility databases is attained to provide energy and diffusivity information during the phase-field simulation. Two different resolutions are used to resolve the primary α-(Al) dendrite and the faceted β-AlFeSi eutectic phase in the phase-field simulations. The phase-field simulated microstructure morphology is verified by experimental results. Moreover, the mechanisms of the characteristic patterns and microstructure formation are demonstrated with the aid of the phase-field simulation. Additionally, the microsegregation and back-diffusion phenomena in the primary α-(Al) dendrite are also analyzed.

The present work demonstrates that the separate phase-field simulations with different resolutions serve as one possibility for continuum description of microstructural evolution in multi-component multi-phase alloys over the entire solidification process, from which the optimal alloy composition may then be designed.

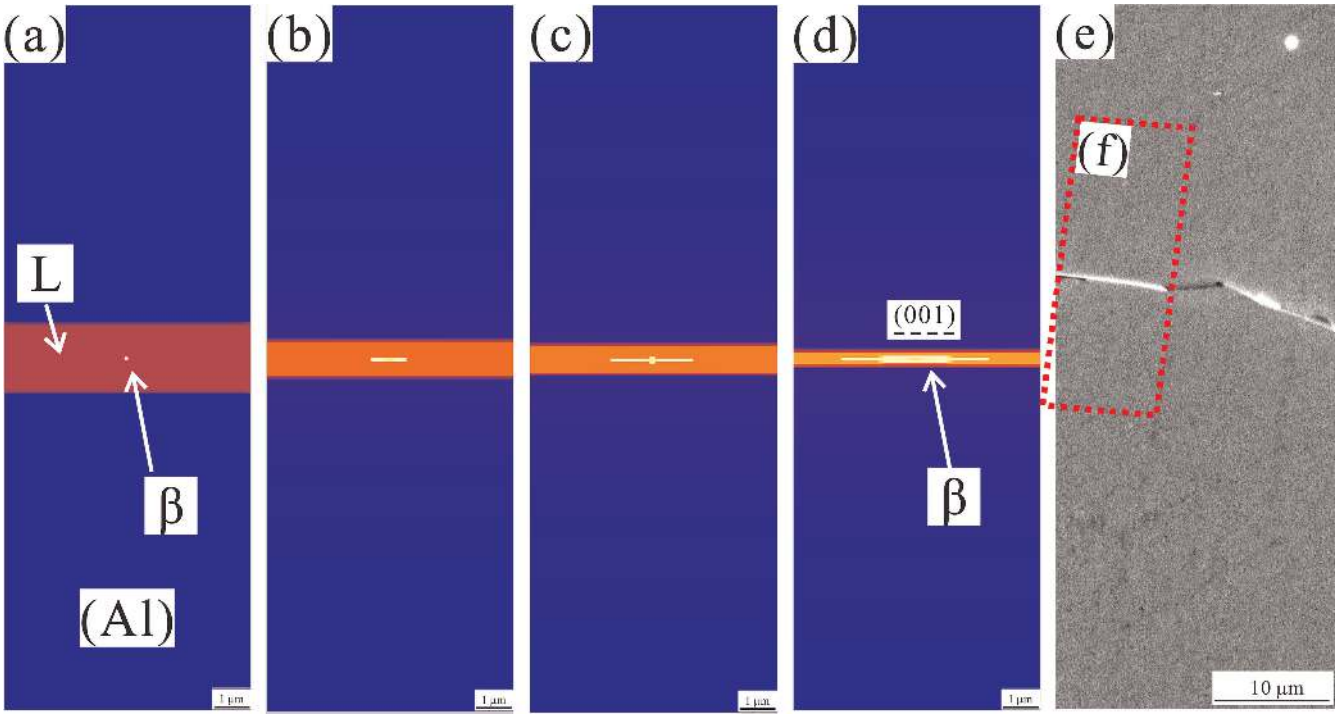

Fig. 6. Phase-field simulation of the faceted growth process of the β-AlFeSi phase. (a) T = 865 K, (b) T = 863 K, (c) T = 855 K, (d) T = 833 K, (e) experimental result.

The work was supported by National Natural Science Foundation of China (Grant Nos. 51531009 and 51474239) and Chinalco Research Institute of Science and Technology Co., Ltd., China. Ming Wei acknowledges support by Fundamental Research Funds for the Central Universities of Central South University (Grant No. 2015zzts185), Changsha, China. Lijun Zhang acknowledges the project supported by State Key Laboratory of Power Metallurgy Foundation, Central South University, Changsha, China.

References

[1] L.F. Mondolfo: Aluminum alloys: structure and properties. Butterworths, London (1976).
[2] I.N. Fridlyander, V.G. Sister, O.E. Grushko, V.V. Berstenev, L.M. Sheveleva, L.A. Ivanova: Met. Sci. Heat Treat. 44 (2002) 365–370. DOI:10.1023/A:1021901715578
[3] J. Hirsch: Trans. Nonferr. Metal Soc. China 24 (2014) 1995–2002. DOI:10.1016/S1003-6326(14)63305-7
[4] O. Engler, J. Hirsch: Mater. Sci. Eng. A 336 (2002) 249–262. DOI:10.1016/S0921-5093(01)01968-2
[5] W.S. Miller, L. Zhuang, J. Bottema, A. Wittebrood, P.D. Smet, A. Haszler, A. Vieregge: Mater. Sci. Eng. A 280 (2000) 37–49. DOI:10.1016/S0921-5093(99)00653-X
[6] O. Engler, E. Brünger: Mater. Sci. Forum 396 (2002) 345–350. DOI:10.4028/www.scientific.net/MSF.396-402.345
[7] A. Kermanpur, M. Eskandari, H. Purmohamad, M.A. Soltani, R. Shateri: Mater. Design 31 (2010) 1096–1104. DOI:10.1016/j.matdes.2009.09.045
[8] X. Wu: Intermetallics 14 (2006) 1114–1122. DOI:10.1016/j.intermet.2005.10.019
[9] B. Dang, C.C. Liu, F. Liu, Y.Z. Liu, Y.B. Li: Trans. Nonferr. Met. Soc. China 26(2016) 634–642. DOI:10.1016/S1003-6326(16)64152-3
[10] V. Hansen, B. Hauback, M. Sundberg, C. Rømming, J. Gjønnes: Acta Crystallogr. B 54 (1998) 351–357. DOI:10.1107/S0108768197017047
[11] R.S. Claves, A.R. Bandar, W.Z. Misiolek, J.R. Michael: Microsco. Microana. 10 (2004) 1138–1139. DOI:10.1017/S1431927604886094
[12] L. Sweet, S.M. Zhu, S.X. Gao, J.A. Taylor, M.A. Easton: Metall. Mater. Trans. A 42 (2011) 1737–1749. DOI:10.1007/s11661-010-0595-6
[13] W.J. Boettinger, J.A. Warren, C. Beckermann, A. Karma: Annu. Rev. Mater. Res. 32 (2002) 163–194. DOI:10.1146/annurev.matsci.32.101901.155803
[14] M. Plapp: J. Cryst. Growth 303 (2007) 49–57. DOI:10.1016/j.jcrysgro.2006.12.064
[15] N. Moelans, B. Blanpain, P. Wollants: CALPHAD 32 (2008) 268–294. DOI:10.1016/j.calphad.2007.11.003
[16] A. Karma, D. Tourret: Curr. Opin. Solid St. M. 20 (2016) 25–36. DOI:10.1016/j.cossms.2015.09.001
[17] I. Steinbach: Modelling Simul. Mater. Sci. Eng. 17 (2009) 073001. DOI:10.1088/0965-0393/17/7/073001
[18] L.J. Zhang, M. Stratmann, Y. Du, B. Sundman, I. Steinbach: Acta Mater. 88 (2015) 156–169. DOI:10.1016/j.actamat.2014.11.037
[19] I. Steinbach, F. Pezzolla, B. Nestler, M. Seeßelberg, R. Prieler, G.J. Schmitz, J.L. Rezende: Physica D 94 (1996) 135–147. DOI:10.1016/0167-2789(95)00298-7
[20] J. Eiken, B. Böttger, I. Steinbach: Phys. Rev. E 73 (2006) 066122. PMid:16906929; DOI:10.1103/PhysRevE.73.066122
[21] web.micress.de (Accessed on 2017-04-27).
[22] S.G. Fries, B. Boettger, J. Eiken, I. Steinbach: Int. J. Mater. Res. 100 (2009) 128–134. DOI:10.3139/146.110013
[23] L.J. Zhang, I. Steinbach, Y. Du: Int. J. Mater. Res. 102 (2011) 371–380. DOI:10.3139/146.110470
[24] L.J. Zhang, Y. Du: J. Phase Equilib. Diff. 37 (2016) 259–260. DOI:10.1007/s11669-015-0422-2
[25] B. Böttger, J. Eiken, I. Steinbach: Acta Mater. 54 (2006) 2697–2704. DOI:10.1016/j.actamat.2006.02.008
[26] B. Böttger, A. Carré, J. Eiken, G.J. Schmitz, M. Apel: Trans. Indian I. Metals 62 (2009) 299–304. DOI:10.1007/s12666-009-0046-5
[27] J. Eiken, M. Apel, S.M. Liang, R. Schmid-Fetzer: Acta Mater. 98 (2015) 152–163. DOI:10.1016/j.actamat.2015.06.056
[28] M. Wei, Y. Tang, L.J. Zhang, Y. Du: Metall. Mater. Trans. A 46 (2015) 3182–3191. DOI:10.1007/s11661-015-2911-7
[29] K. Wang, M. Wei, L. Zhang, Y. Du: Metall. Mater. Trans. A 47 (2016) 1510–1516. DOI:10.1007/s11661-016-3358-1
[30] R.F. Almgren: J. Appl. Math. 59 (1999) 2086–2107. DOI:10.1137/S0036139997330027
[31] A. Karma, W.J. Rappel: Phys. Rev. E 53 (1996) R3017. PMid:9964755; DOI:10.1103/PhysRevE.53.R3017
[32] A.M. Mullis, J. Rosam, P.K. Jimack: J. Cryst. Growth 312 (2010) 1891–1897. DOI:10.1016/j.jcrysgro.2010.03.009
[33] A. Karma: Phys. Rev. Lett. 87 (2001) 115701. DOI:10.1103/PhysRevLett.87.115701
[34] S.G. Kim: Acta Mater. 55 (2007) 4391–4399. DOI:10.1016/j.actamat.2007.04.004
[35] A. Gopinath, R.C. Armstrong, R.A. Brown: J. Cryst. Growth 291 (2006) 272–289. DOI:10.1016/j.jcrysgro.2006.03.001
[36] M. Ohno, K. Matsuura: Phys. Rev. E 79 (2009) 031603. PMid:19391950; DOI:10.1103/PhysRevE.79.031603
[37] S.Y. Pan, M.F. Zhu: Acta Mater. 58 (2010) 340–352. DOI:10.1016/j.actamat.2009.09.012
[38] A. Carre, B. Bottger, A. Apel: J. Cryst. Growth 380 (2013) 5–13. DOI:10.1016/j.jcrysgro.2013.05.032
[39] G. Boussinot, E.A. Brener: Phys. Rev. E 88 (2013) 022406. PMid:24032848; DOI:10.1103/PhysRevE.88.022406
[40] A. Fang, Y. Mi: Phys. Rev. E 87 (2013) 012402. PMid:23410339; DOI:10.1103/PhysRevE.87.012402
[41] Y. Du, S. Liu, L.J. Zhang, H. Xu, D. Zhao, A. Wang: CALPHAD 35 (2011) 427–445. DOI:10.1016/j.calphad.2011.06.007
[42] Y. Du, L.J. Zhang, S. Cui, D. Zhao, D. Liu, W. Zhan, W. Sun, W. Jie: Sci. China Tech. Sci. 55 (2012) 306–27. DOI:10.1007/s11431-011-4692-6
[43] L.J. Zhang, D. Liu, W. Zhang, S. Wang, Y. Tang, N. Ta, M. Wei, Y. Du: Mater. Sci. Forum 794–796 (2014) 611–616. DOI:10.4028/www.scientific.net/MSF.794-796.611
[44] M. Gündüz, J.D. Hunt: Acta Metall. 33 (1985) 1651–1672. DOI:10.1016/0001-6160(85)90161-0
[45] W. Khalifa, A.M. Samuel, F.H. Samuel, H.W. Doty, S. Valtierra: Int. J. Cast Metal Res. 19 (2006) 156–166. DOI:10.1179/136404606225023372
[46] G. Sha, K. O'Reilly, B. Cantor: Mater. Sci. Forum 519 (2006) 1721–1726. DOI:10.4028/www.scientific.net/MSF.519-521.1721
[47] S. Terzi, J.A. Taylor, Y.H. Cho, L. Salvo, M. Suéry, E. Boller, A.K. Dahle: Acta Mater. 58 (2010) 5370–5380. DOI:10.1016/j.actamat.2010.06.012

(Received June 5, 2017; accepted August 15, 2017; online since November 27, 2017)

Correspondence address

Prof. Dr. Lijun Zhang
State Key Lab of Powder Metallurgy
Central South University
Changsha 410083
P. R. China
Tel.: +86 731 88877963
Fax: +86 731 88710855
E-mail: xueyun168@gmail.com
lijun.zhang@csu.edu.cn

Bibliography
DOI 10.3139/146.111584
Int. J. Mater. Res. (formerly Z. Metallkd.)
109 (2018) 2; page 91–98

ISSN 1862-5282